Chemical Science

ROYAL SOCIETY OF CHEMISTRY

EDGE ARTICLE

View Article Online
View Journal | View Issue

Cite this: *Chem. Sci.*, 2022, **13**, 81

All publication charges for this article have been paid for by the Royal Society of Chemistry

Received 3rd September 2021
Accepted 2nd November 2021

DOI: 10.1039/d1sc04883j

rsc.li/chemical-science

Supramolecular polymerization of electronically complementary linear motifs: anti-cooperativity by attenuated growth†

Yeray Dorca,‡[a] Cristina Naranjo, ‡[a] Goutam Ghosh, [b] Bartolomé Soberats, [c] Joaquín Calbo, [d] Enrique Ortí, *[d] Gustavo Fernández *[b] and Luis Sánchez *[a]

Anti-cooperative supramolecular polymerization by attenuated growth exhibited by self-assembling units of two electron-donor benzo[1,2-*b*:4,5-*b*′]dithiophene (BDT) derivatives (compounds **1a** and **1b**) and the electron-acceptor 4,4-difluoro-4-bora-3*a*,4*a*-diaza-*s*-indacene (BODIPY) (compound **2**) is reported. Despite the apparent cooperative mechanism of **1** and **2**, AFM imaging and SAXS measurements reveal the formation of small aggregates that suggest the operation of an anti-cooperative mechanism strongly conditioned by an attenuated growth. In this mechanism, the formation of the nuclei is favoured over the subsequent addition of monomeric units to the aggregate, which finally results in short aggregates. Theoretical calculations show that both the BDT and BODIPY motifs, after forming the initial dimeric nuclei, experience a strong distortion of the central aromatic backbone upon growth, which makes the addition of successive monomeric units unfavourable and impedes the formation of long fibrillar structures. Despite the anti-cooperativity observed in the supramolecular polymerization of **1** and **2**, the combination of both self-assembling units results in the formation of small co-assembled aggregates with a similar supramolecular polymerization behaviour to that observed for the separate components.

Introduction

Inspired by the basic knowledge and the practical applicability of covalent polymers, and relying on seminal studies reporting the stable interaction between complementary self-assembling units, the field of supramolecular polymers has witnessed a spectacular evolution in the last few decades.[1–4] The expansion of the field has greatly benefited from the introduction of innovative molecular design strategies as well as the development of both experimental techniques and theoretical models, which have contributed to the elucidation of structure–function relationships and the subsequent application of such systems.[1–4] A key step in the controlled formation of supramolecular polymers stemmed from the elaboration of models suitable to disentangle the self-assembly mechanism, mainly isodesmic or cooperative. The former is defined by only one binding constant, whilst the latter encompasses two regimes, nucleation and elongation, with the corresponding binding constants.[1] Exciting phenomena addressed to achieve functional supramolecular polymers rely on cooperativity. Thus, research on kinetically controlled, cooperative aggregation processes paved the way to increase the complexity level in this field.[5–9] Motivated by the pioneering reports on crystallization-driven self-assembly,[10] a number of cooperative systems undergoing seeded and living supramolecular polymerizations have been reported.[11–16]

A further step in the achievement of functional supramolecular polymers is the controlled synthesis of block supramolecular polymers (BSPs), where different monomers interact *via* noncovalent interactions.[17] A number of examples of supramolecular copolymers with defined alternating,[18,19] periodic,[20] or block[21–23] microstructures have been achieved by rational monomer design. However, controlling the segmented microstructure of BSPs into functional architectures is a formidable challenge, to which considerable efforts have been devoted in recent years.[17] Kinetically driven supramolecular polymerization approaches have been successfully used to yield supramolecular polymers with controlled microstructures. For instance, several dye molecules including hexabenzocoronenes, porphyrins, core-substituted perylene bisimides or fluorescent naphthalene bisimides have been reported to form BSPs in a controlled fashion.[22,24–26] Together with these strategies, and

[a]*Departamento de Química Orgánica, Facultad de Ciencias Químicas, Universidad Complutense de Madrid, Ciudad Universitaria, s/n, 28040, Madrid, Spain. E-mail: lusamar@ucm.es*

[b]*Organisch-Chemisches Institut Westfälische Wilhelms, Universität Münster, Corrensstraße 36, 48149 Münster, Germany. E-mail: fernandg@uni-muenster.de*

[c]*Department of Chemistry, University of the Balearic Islands, Cra. Valldemossa, Km. 7.5, 07122, Palma de Mallorca, Spain*

[d]*Instituto de Ciencia Molecular (ICMol), Universidad de Valencia, C/Catedrático José Beltrán, 2, 46980 Paterna, Spain. E-mail: enrique.orti@uv.es*

† Electronic supplementary information (ESI) available. See DOI: 10.1039/d1sc04883j

‡ These authors contributed equally.

inspired by the covalent chain-growth copolymerization, recent examples of cooperative, thermodynamically controlled supramolecular copolymers have been reported.[23,27]

In contrast to the isodesmic and cooperative supramolecular polymerization mechanisms, in which the degree of cooperativity σ is equal to unity or lower than unity, respectively, the occurrence of an anti-cooperative mechanism has been much less investigated. In an anti-cooperative mechanism, which features a value for $\sigma > 1$, the formation of small aggregates is more favoured than large supramolecular structures.[28–31] Among the scarce examples of anti-cooperative mechanisms, the formation of very stable dimers is very often the key step in the final mechanistic outcome. However, there are very few examples of anti-cooperative mechanisms directed by attenuated growth.[32] In one of these examples, the propensity of a perylene bisimide (PBI) dimer to be added to the aggregate decreases upon increasing the aggregate size. Thus, the non-sigmoidal shape of the corresponding melting curves, ascribable in principle to a typical cooperative mechanism into long supramolecular polymers, contrasts with the small size of the aggregates derived from small angle X-ray scattering (SAXS) measurements.[32c] To date, charge repulsion,[32a] steric effects between dendritic water-soluble chains[32b] or the formation of stable hydrogen-bonded dimers[32c] have been identified as key factors determining attenuated growth in anti-cooperative self-assembly.

In this article, we reveal that peripheral alkyl chains, which are commonly employed structural elements of self-assembling monomers, can induce anti-cooperative effects and frustrated growth in supramolecular polymerization. To achieve this goal, we designed two geometrically and electronically complementary monomer units bearing amide groups as well as solubilizing alkoxy chains (Fig. 1). The selected monomers [the electron-donor (p-type) benzo[1,2-*b*:4,5-*b*′]dithiophene (BDT) (compounds **1a** and **1b**) and the electron-acceptor (n-type) 4,4-difluoro-4-bora-3*a*,4*a*-diaza-*s*-indacene (BODIPY) (compound **2**)] have been widely used in the field of organic photovoltaics or as biolabels, laser dyes and photodynamic therapy agents.[33–35] Variable-temperature (VT) UV-Vis experiments show non-sigmoidal melting curves indicative of a cooperative mechanism. However, both atomic force microscopy (AFM) imaging and SAXS measurements reveal the formation of small aggregates. These counterintuitive findings are attributed to an anti-cooperative mechanism strongly conditioned by an attenuated growth in which the formation of a small supramolecular nucleus is favoured over the subsequent addition of monomer units to the aggregate finally yielding short assemblies (Fig. 1b). Theoretical calculations show the strong influence of the peripheral side chains on the supramolecular polymerization of both the BDT and BODIPY motifs. Thus, upon formation of the initial dimeric nuclei with an antiparallel arrangement of the self-assembling units, further addition of monomer units to the aggregate results in a strong distortion of the central aromatic core that destabilizes the resulting supramolecular polymer and impedes the formation of long fibrillar structures (Fig. 1b). Despite the anti-cooperativity observed in the supramolecular polymerization of the reported BDT and BODIPY derivatives, the combination of both self-assembling units results in the formation of co-assembled aggregates that exhibit a supramolecular polymerization behaviour similar to that observed for the separate components. The results here presented contribute to expanding the knowledge on anti-cooperative supramolecular polymerization and, at the same time, provide a useful chemical approach to achieve functional oligomeric species *a-la-carte*, thus bridging the molecular and macromolecular levels.

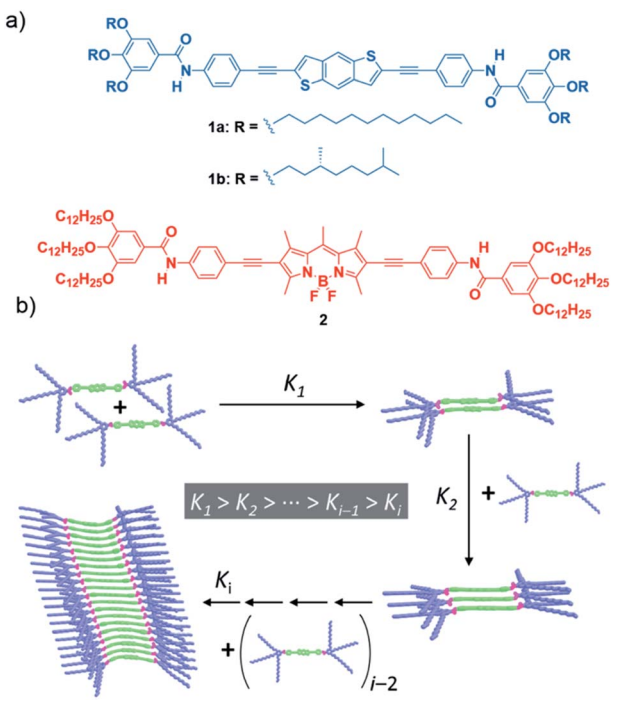

Fig. 1 (a) Chemical structure of achiral BDT **1a**, chiral BDT **1b**, and BODIPY **2**. (b) Schematic illustration of the anti-cooperative supramolecular polymerization of **1** by attenuated growth. This schematic illustration is also valid for compound **2**.

Results and discussion

Synthesis and supramolecular polymerization

The target BDT derivatives **1** were prepared by following a synthetic methodology analogous to that used for the previously reported BODIPY derivative **2**.[36] The key step in the synthetic procedure implies the twofold C–C cross-coupling Sonogashira reaction between the commercially available 2,6-dibromobenzo[1,2-*b*:4,5-*b*′]dithiophene and *N*-(4-ethynylphenyl)-3,4,5-trimethoxybenzamide (**7**),[36] affording **1a** and **1b** in 86 and 65% yield, respectively (Scheme S1, ESI†). The spectroscopic data confirm the chemical structure of **1** (see ESI for details†).

A detailed study of the supramolecular polymerization of achiral **1a**, chiral **1b** and **2** is required prior to the investigation of the co-assembly of these complementary BDT and BODIPY derivatives. This preliminary study was carried out by VT-UV-Vis measurements in methylcyclohexane (MCH) as solvent (for details about the sample preparation, see ESI†). The UV-Vis

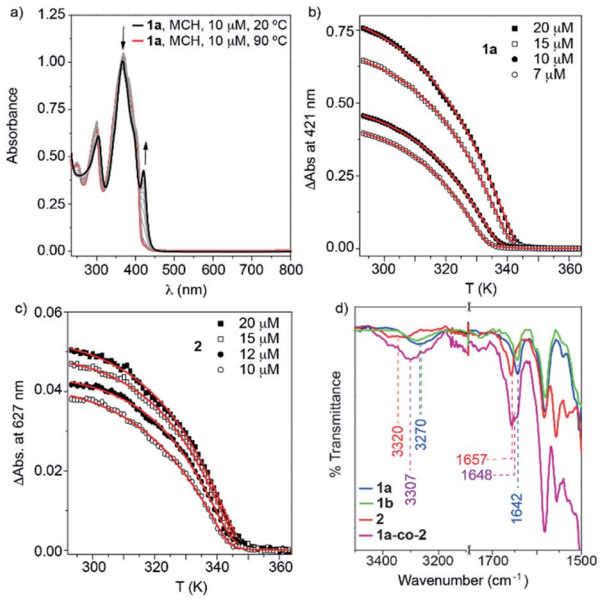

Fig. 2 (a) UV-Vis spectra of **1a** at different temperatures (MCH, $c_T = 10$ μM). Arrows indicate the changes in the absorption bands upon decreasing the temperature. (b and c) Cooling curves (1 K min^{-1}) of **1a** (b) and **2** (c) in MCH at different concentrations. Red lines in (b) and (c) depict the fitting to the one-component EQ model. (d) Partial FTIR spectra of **1a** (blue), **1b** (green), **2** (red) and **1a-co-2** (magenta) in MCH solution at $c_T = 1$ mM showing the N–H stretching and amide I bands.

spectrum of achiral **1a** at 20 °C shows two bands at 304 and 367 nm, two shoulders at 385 and 402 nm and a well-defined, narrow peak at 421 nm (Fig. 2a). Heating this solution to 90 °C transforms this absorption pattern into a slightly sharper and more intense UV-Vis spectrum, with maxima at 301 and 371 nm, where the shoulder is shifted to 405 nm and the peak at 421 nm is absent (Fig. 2a). The absorption pattern of **1a** at 90 °C coincides with that observed in $CHCl_3$ at 20 °C, indicating a molecularly dissolved state (Fig. S1, ESI†). Notably, the fact that the main absorption band negligibly shifts upon aggregation in MCH ($\Delta\lambda = -4$ nm, see Fig. 2a) suggests the occurrence of weak exciton coupling of the BDT chromophores, *i.e.* no-typical H- or J-type aggregates. On the other hand, the emergence of a red-shifted shoulder band at 421 nm for the solution at 20 °C may result from a weak rotational offset of the chromophores within the columnar stacks.[36,37] Identical absorption features have been observed for chiral **1b** (Fig. S2, ESI†). Plotting the increase of the absorption peak at 421 nm upon decreasing temperature at different concentrations for BDT derivatives **1a** and **1b** displays non-sigmoidal curves with a clear critical temperature (temperature of elongation, T_e) ascribable to a cooperative supramolecular mechanism (Fig. 2b and S2,† respectively).[1] The global fitting of these curves to the one-component version of the equilibrium (EQ) model[38] affords a complete set of thermodynamic parameters associated with the thermodynamically controlled supramolecular polymerization of **1** (Table S1, ESI†).

On the other hand, BODIPY derivative **2** has been previously described to form H-type aggregates following a cooperative mechanism.[36] In this case, decreasing the temperature is accompanied by the depletion of the absorption maximum at 576 nm and the rise of a band at 540 nm (Fig. S3a, ESI†).[36] To have a coherent estimation of the thermodynamic parameters for both self-assembling units, the non-sigmoidal curves obtained by plotting the variation of the shoulder at 627 nm were also fitted to the one-component EQ model (Fig. 2c). The elongation temperature (T_e), for compound **2** is higher than that derived for the BDT derivatives **1**, which implies the higher stability of the BODIPY derivative in comparison to the BDT derivatives (Table S1, ESI†).[1]

Our previous report on the self-assembly of the BODIPY derivative **2** demonstrates that the synergy of hydrogen bonding (H-bonding) interactions, taking place between amide functional groups, and the π-stacking of the aromatic moieties justify the cooperative formation of H-type aggregates.[36] In good analogy, the supramolecular polymers of BDT derivatives **1a** and **1b** are expected to involve the operation of H-bonding interactions between amide groups and the π-stacking of the BDT cores. This hypothesis is corroborated by FTIR studies performed in MCH at a total concentration (c_T) of 1 mM. The FTIR spectra of **1** and **2** show the N–H (3270/3320 cm^{-1}) and the amide C=O (1642/1657 cm^{-1}) stretching bands at wavenumbers ascribed to H-bonded amides (Fig. 1d and S4, ESI†).[9,39,40] These wavenumbers contrast with those recorded for compounds **1** and **2** in $CHCl_3$ at the same c_T (1 mM). In this good solvent, the N–H and amide C=O bands appear at 3430 and 1675 cm^{-1} for both **1** and **2** (Fig. S4, ESI†), confirming that $CHCl_3$ favours a complete molecularly dissolved state. It is noteworthy that the wavenumbers observed for the N–H and amide I stretching bands in MCH for **1** (3270 and 1642 cm^{-1}) are slightly lower than those registered for **2** (3320 and 1657 cm^{-1}), which indicates weaker H-bonding interactions for the BODIPY derivative. The shape and size of both self-assembling units (33.4 and 33.1 Å for the BDT- and BODIPY-based linear moieties, respectively, Fig. S5, ESI†) are comparable and, therefore, the strength of π-stacking is expected to be similar. However, the higher stability of **2** can be explained by the known tendency of BODIPY to stack with the BF_2 groups alternately pointing to opposite sides. This disposition enables further stabilization gain *via* short F···H contacts and C–H···π interactions.[41,42]

According to the combined experimental evidence and, very especially, taking into account the cooperative mechanism governing the supramolecular polymerization of compounds **1** and **2**, the formation of long fibrillar aggregates should be expected. To visualize the morphology of the supramolecular polymers formed, AFM images were registered by depositing diluted solutions ($c_T = 25$ μM) of compounds **1** and **2** in MCH onto mica as the surface. To our surprise, the AFM images of all three self-assembling units show short, worm-like aggregates with typical heights of ~2 nm (Fig. 3 and S6, ESI†). Although the height is in good accordance with the length of the rigid part of both the BDT and BODIPY cores (Fig. S5, ESI†), the length of the aggregates experimentally measured is significantly shorter than expected, considering a cooperative supramolecular mechanism.[8–13]

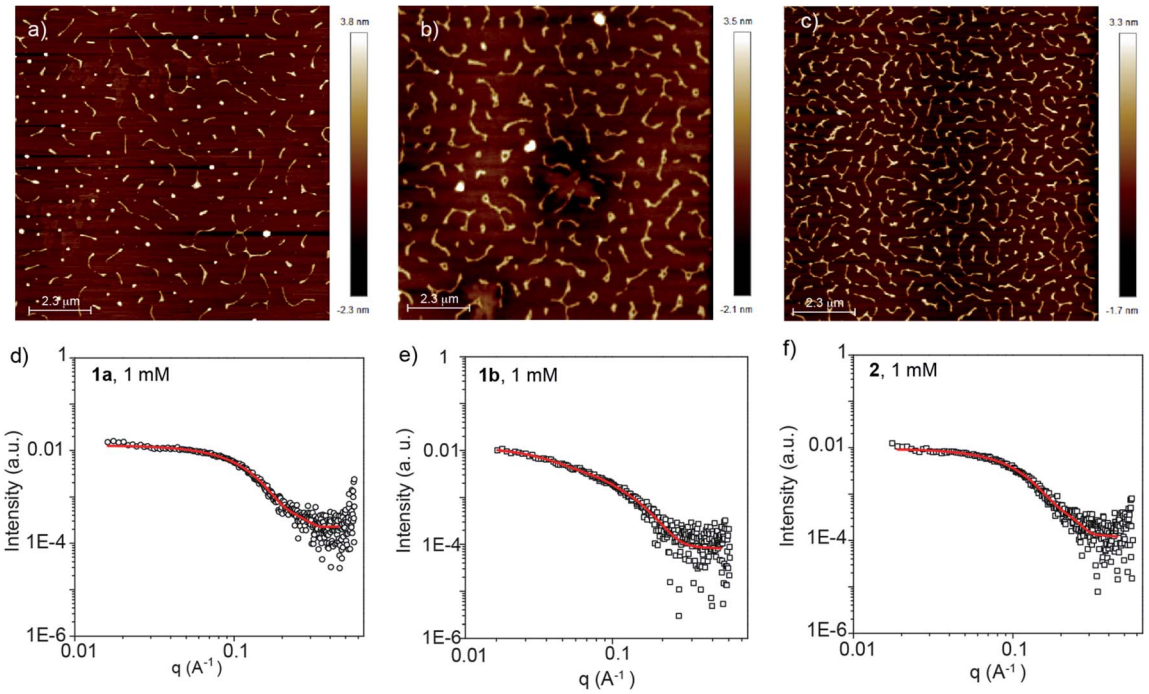

Fig. 3 (a–c) Height AFM images of **1a** (a), **1b** (b) and **2** (c). Experimental conditions for AFM imaging: mica as surface, MCH, $c_T = 25$ μM, spin coating. (d–f) SAXS data and fitting for **1a** (d), **1b** (e) and **2** (f). Red lines in (d and e) depict the fitting to the elliptical cylinder model (experimental conditions: MCH as solvent, $c_T = 1$ mM).

The self-assembly of BDTs **1a** and **1b** as well as BODIPY **2** in solution was further investigated by small angle X-ray scattering (SAXS) measurements. The SAXS profiles were obtained from MCH solutions of **1a**, **1b** and **2** ($c_T = 1$ and 2.5 mM) and fitted using different customized models (Fig. 3d–f and S7, ESI†). The experimental SAXS profiles were found to fit best with form factors of monodisperse elliptical cylinders[43] with a minor radius of ~1 nm and axis ratios of ~2 (see Table S2, ESI†), which is consistent with the molecular shape of the rigid part of the monomers. Remarkably, these fittings also reveal unusual short lengths of the polymers, which range between 3.2 and 4.5 nm for **1a** and **2**. In the case of chiral **1b**, the aggregates are slightly longer with lengths of 10–12 nm. On the basis of these results, and considering a typical distance between molecules of 3.4 Å, it is apparent that the aggregates formed from the reported self-assembling units consist of short elliptical cylinder assemblies composed of 10–13 monomeric units for **1a** and **2**, and 35 units for chiral **1b**. The diameter and lengths calculated by SAXS experience no remarkable changes upon increasing the concentration (Fig. S7 and Table S2, ESI†). Importantly, these values are significantly lower than those expected by taking into account the cooperative supramolecular polymerization mechanism, the corresponding derived thermodynamic parameters (Table S1, ESI†), and the concentration range utilized in the SAXS measurements (two orders of magnitude higher than that used in the corresponding VT-UV-Vis experiments).

These opposite findings have been previously described for asymmetric PBIs able to form dimers that further interact to form small aggregates.[32] In this system, the addition of a limited number of monomer units to the initially formed nuclei is favoured. However, the further growth of the polymer chain is impeded, most probably due to steric effects. The result is an anti-cooperative supramolecular polymerization by attenuated growth that, however, presents non-sigmoidal melting curves.

On the origin of anti-cooperativity by attenuated growth. Computational modelling

Theoretical calculations were performed on the columnar assemblies of BDT **1** and BODIPY **2** to shed light on the supramolecular polymerization mechanism that leads to the formation of such unexpected short fibers (see the ESI† for computational details). Preliminary calculations at the cost-effective GFN2-xTB semiempirical level were performed to assess the thermodynamic stability towards the formation of dimeric species.[44,45] Among the different possible supramolecular dimers, those in which the BDT and BODIPY aromatic cores are alternately stacked, pointing in opposite directions thus minimizing S···S and F···F steric clashes, respectively, are predicted as the most stable configurations (Fig. 4, S8 and S9 and Table S3, ESI†), in good accordance with reported crystal data on related compounds.[41,42] As a result, dimers of **1** and **2** are predicted with a large binding energy of −52.2 and −56.9 kcal mol^{-1}, respectively, thus supporting the favourable nucleation process experimentally found in the supramolecular polymerization of BDT- and BODIPY-based linear motifs.

The most stable dimer aggregates for BDT **1** and BODIPY **2** derivatives were used to build supramolecular fibres of increasing size up to 30 units (*ca.* 11 nm of length along the growing axis) both without and with peripheral aliphatic

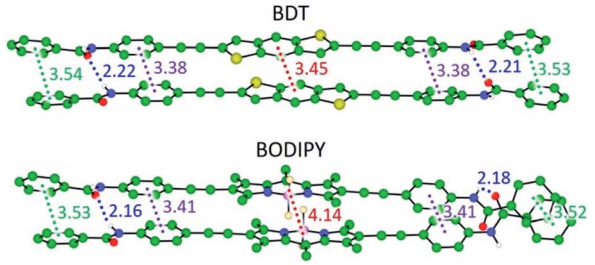

Fig. 4 Minimum-energy geometries calculated at the GFN2-xTB level of theory for the most stable arrangement in dimeric species of BDT **1** and BODIPY **2** without peripheral aliphatic chains. Relevant intermolecular distances are indicated in Å. A sliding shift of *ca.* 1.4 Å is calculated in both dimers along the long molecular axis. Colour coding: C in green, N in blue, O in red, S in yellow, B in pink, F in pale yellow and H in white. Hydrogens attached to carbons are omitted for clarity.

chains. Fully-optimized supramolecular structures of **1** confirm that the linear BDT core can easily stack linearly forming long fibres while preserving the core-to-core π–π interactions and the H-bonding network between the amide groups (Fig. 5a).

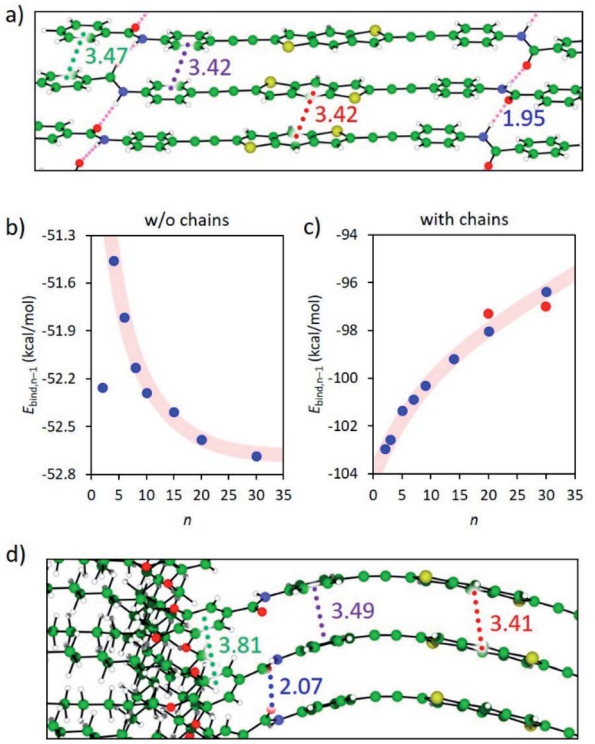

Fig. 5 (a) Relevant intermolecular mean distances (in Å) calculated for the minimum-energy structure of a decamer of **1** without peripheral aliphatic chains. (b and c) Evolution of the binding energy per interacting pair as a function of the number of monomers (*n*) in the aggregate calculated for the most stable arrangement of **1** without (b) and with (c) peripheral aliphatic achiral chains. Transparent red lines are drawn to guide the eye. Red data in (c) correspond to central-disrupted oligomer stacks. (d) Relevant intermolecular mean distances (in Å) calculated for the minimum-energy structure of a decamer of **1** with peripheral aliphatic chains (**1a**).

Despite the slight increase of the binding energy per interacting pair ($E_{bind,n-1}$) calculated in going from the dimer to the trimer species (Fig. 5b), an exponential decay of $E_{bind,n-1}$, typical of a cooperative polymerization mechanism, is predicted for **1** upon increasing the aggregate size when peripheral alkyl chains are not considered and regardless of the parallel or antiparallel arrangement of the BDT units (Fig. 5b, S10a–S12a, ESI†). Interestingly, this cofacial, slightly long-axis slipped stacking leading to a weakly directional hydrogen-bonding network pattern with H-bond contacts of 2.1–2.3 Å, in combination with short π–π interactions in the range of 3.2–3.7 Å, is favoured with respect to a helical growth with linear H-bonds (Fig. S8, S11b and S12b, ESI†).[46]

In sharp contrast, the introduction of the long aliphatic chains in terminal positions of **1** leads to a completely different behavior, with a gradual increase of $E_{bind,n-1}$ upon increasing the fibre length (Fig. 5c). A careful inspection of the geometry of the stacks shows that the peripheral groups promote steric clashes that lead to a difference in the separation between neighboring core-to-core and peripheral benzene-to-peripheral benzene units (intermolecular mean distances of 3.41 and 3.81 Å, respectively; Fig. 5d and S14a†). This steric hindrance accumulates and increases the deformation from coplanarity of the linear BDT-based building blocks of **1** upon fibre growth, thus explaining the progressive destabilization of the stack with the aggregate size. Furthermore, the increasing π–π distances upon aggregate growth agree with the experimentally observed weak exciton coupling leading to negligible shifts in the main absorption band upon aggregation (see Fig. 2a).

On the other hand, preliminary quantum chemical calculations (PBEh-3c/HF-3c + COSMORS) were reported to examine the formation of dimers and tetramers of **2**, where the long dodecyloxy chains were removed. Even though the formation of tetramers was predicted to be exothermic (−2.6 kcal mol^{-1}), a slight zigzag-like arrangement of the BODIPYs and some steric interactions were noticed. In order to better understand the correlation between the structural aspects and the self-assembly mechanism, we performed theoretical calculations for columnar assemblies of **2** with a variable number of monomers from the dimer to the 20-mer, with and without peripheral chains. Notably, the bulky BODIPY core promotes a steric congestion in the supramolecular stacking of **2**, which accumulates upon fibre growth, with a core-to-core intermolecular mean distance of 3.90 Å (Fig. S10b, ESI†). As a result, even without the presence of peripheral aliphatic chains, the binding energy per interacting pair increases gradually upon increasing the aggregate size (Fig. S15a, ESI†), indicative of an anti-cooperative growth. The inclusion of the peripheral long alkyl chains maintains the $E_{bind,n-1}$ trend (Fig. S15b, ESI†), and promotes additional steric clashes in the periphery of the linear BODIPY-based motif, which results in a wavy distortion of the stack (Fig. S16a, ESI†). The theoretical results obtained for both **1** and **2** therefore support the anti-cooperative supramolecular polymerization by attenuated growth sketched in Fig. 1b and proposed experimentally for both systems.

To relieve part of the core distortion suffered upon polymerization growth, hypothetical assemblies of BDT **1** and

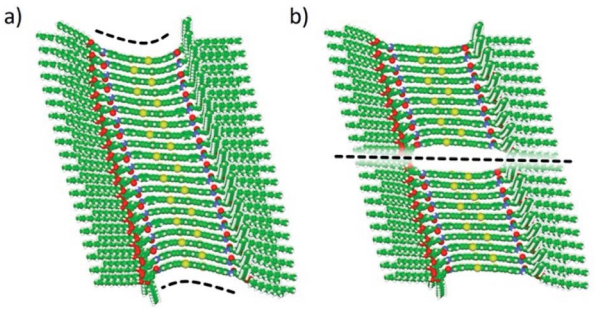

Fig. 6 Minimum-energy structures calculated for a highly-distorted fully-interacting (a) and a central-disrupted (b) 20-mer of BDT **1a** with peripheral aliphatic chains.

BODIPY **2**, where two central units are not interacting, were also modelled. Theoretical calculations indicate that the geometry deformation penalty release can compete in energy with the stabilizing π–π core-to-core and H-bonding interactions in large oligomers. Very small energy differences are indeed predicted between a fully-interacting aggregate and a central-disrupted stack: $E_{\mathrm{bind},n-1}$ of −98.0 and −97.3 kcal mol^{-1}, respectively, for a 20-mer of **1a** (Fig. 6), and $E_{\mathrm{bind},n-1}$ of −96.9 and −96.2 kcal mol^{-1}, respectively, for a 20-mer of **2** (Fig. S16, ESI†). In fact, a disrupted stack of 30 units of **1a** is favoured ($E_{\mathrm{bind},n-1} = -97.0$ kcal mol^{-1}) over the fully core-to-core interacting analogue ($E_{\mathrm{bind},n-1} = -96.4$ kcal mol^{-1}). Theoretical calculations on the self-assembly of our linear motifs **1** and **2** therefore suggest that when the oligomer size is large enough, between 20 and 30 units approximately, the stacking disruption is thermodynamically favoured, leading to separate shorter fibres of 10–15 units, in excellent agreement with the experimental findings.

Experimental study of the coassembly

Despite the anti-cooperative mechanism exhibited by pristine **1a**, **1b** and **2**, the electronic and geometrical complementarity displayed by the electron-donating BDT derivatives **1a** and **1b** and the electron-accepting BODIPY-based **2** prompted us to investigate the coassembly of these units. Photoluminescence studies were initially employed to investigate the formation of coassembled species between **1a** and **2** since aggregates of **2** were previously investigated by this technique,[36] and also because emission is a useful strategy to evaluate the formation of block supramolecular polymers.[23,27,47]

A diluted solution (c_T = 10 μM) of **2** in MCH at room temperature features an emission maximum at 637 nm that strongly increases in intensity and shifts hypsochromically (613 nm) upon heating to 90 °C (Fig. S17, ESI†). In the case of **1a**, the emission spectrum (MCH, c_T = 10 μM, 20 °C) displays a broad band centered at 492 nm that shifts hypsochromically showing a very intense, structured emission pattern upon heating to 90 °C (Fig. S18, ESI†). A highly diluted solution (c_T = 1 μM) of **1a** is required to achieve a complete emission spectrum at high temperature. This 1 μM solution also shows a broad band centered at 492 nm that, upon heating to 90 °C, changes to an intense spectrum with maxima at 437 and 412 nm. This emission pattern coincides with that observed for **1a** in $CHCl_3$ indicating that under these conditions the sample is molecularly dissolved (Fig. S18, ESI†).[35] These emission features corroborate that both **1a** and **2** provide aggregates with an aggregation quenching effect (AQE).

To investigate the co-assembly of **1a** and **2**, we made use of UV-Vis absorption and emission spectroscopies. First, an equimolar mixture of **1a** and **2** in MCH and at c_T = 10 μM, which implies a final monomer concentration of 20 μM, was prepared. This mixture was heated up to 90 °C to reach the molecularly dissolved state of both **1a** and **2** and, subsequently, cooled to 20 °C at 1 K min^{-1} to ensure the formation of thermodynamically controlled aggregates. Fig. S19 (ESI†) displays the minute changes experienced by the mixture before and after the heating/cooling cycle as well as after 72 hours, which indicates that the co-assembly occurs under thermodynamic control. After that, we prepared mixtures of **1a** and **2** at different ratios. The resulting UV-Vis and emission spectra are a superimposition of those registered for the individual components, where the spectroscopic features of each component linearly increase with the amount of added species (Fig. S20, ESI†). The electronic complementarity of **1a**, acting as an electron donor, and **2**, as an electron acceptor, could in principle result in new bands in the UV-Vis/emission spectra due to charge or energy transfer processes in the ground and/or excited states,[48,49] which, unfortunately, are not observed. However, a simple comparison of the equimolar mixture solution of **1a** and **2** (from now on **1a-co-2**) with the naked eye shows an enhanced emission for the co-assembled structure in comparison with the pristine components (Fig. 7a). This may be explained by the difficulty of **2** to undergo face-to-face stacking efficiently in the presence of **1**, therefore disfavouring the formation of non-emissive H-type aggregates, as was the case for the aggregates of **2** in isolation.

The emission spectrum of the mixture of **1a** and **2** at 90 °C in MCH shows an intense structured pattern observed for the molecularly dissolved BDT derivative and a residual emission at 613 nm ascribable to the BODIPY monomeric species (Fig. 7b). Cooling this solution to 20 °C results in the depletion of the emission bands corresponding to the BDT core. Concomitantly, a broad low-intense band centred at 482 nm with residual emission at 440 and 412 nm appears and the band at 606 nm significantly grows in intensity. All these emission maxima are hypsochromically shifted in comparison to the values measured for pristine aggregated **1a** and **2** (compare Fig. 7b, S17 and S18, ESI†). These emission features, with an intense emission band at wavelengths close to the monomeric BODIPY dyes, are taken as a first indication of the formation of BDT-BODIPY junctions in **1a-co-2**. An additional indication of the formation of **1a-co-2** is obtained from FTIR studies in MCH. FTIR spectra show the N–H and amide I stretching bands at 3307 and 1648 cm^{-1}, respectively. These values, indicative of the formation of H-bonding arrays between the amide functional groups, are intermediate between those observed for **1a** and **2** (Fig. 2d). Importantly, the formation of **1a-co-2** in MCH solution was also corroborated by VT-UV-Vis experiments. The cooling curves of equimolar mixtures of **1a** and **2** exhibit only one nucleation–

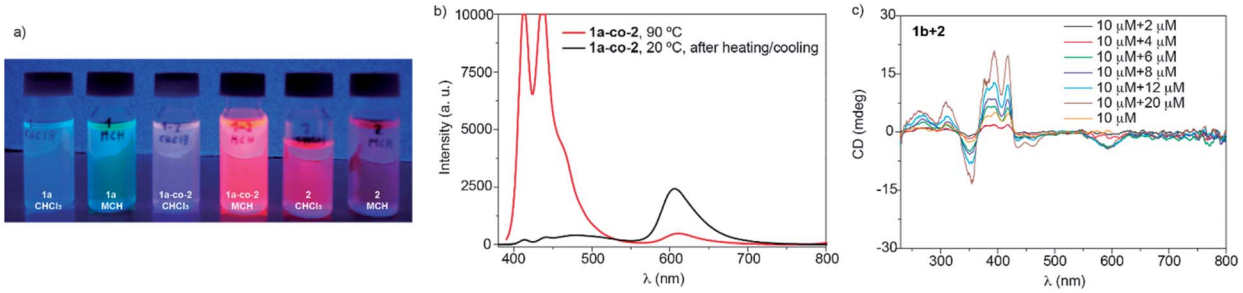

Fig. 7 (a) Picture of solutions of the monomeric and aggregated species of **1a**, **2** and **1a-co-2** in $CHCl_3$ and MCH under irradiation at 364 nm (c_T = 10 μM). (b) Emission spectra of **1a-co-2** in MCH at different temperatures and times (c_T = 10 μM; λ_{exc} = 367 nm). (c) CD spectra of pristine **1b** and mixtures of **1b** and **2** at different ratios (MCH, c_T of **1b** = 10 μM).

elongation transition regardless of the concentration utilized (Fig. S21, ESI†). The lack of two independent nucleation–elongation transitions, at T_e values close to those observed for pristine **1a** and **2**, supports the formation of **1a-co-2**.[17]

A further proof of the co-assembly of the BDT and BODIPY derivatives was accomplished by utilizing the chiral BDT **1b**. Compound **1b** in MCH and at c_T = 10 μM displays a dichroic response with maxima at 464, 444, 419, 395 and 350 nm and two zero-crossing points at 430 and 366 nm (Fig. 7c and S22a, ESI†). Mixing chiral **1b** with achiral **2** at different ratios results in CD spectra with a dichroic pattern similar to that observed for pristine **1b**. Interestingly, the CD spectra of these mixtures also present a dichroic band at 595 nm (Fig. 7c). This wavelength, which does not correspond to the absorption of the BDT core but is ascribable to the absorption of the BODIPY moiety, is indicative of an efficient transfer of asymmetry from chiral **1b** to achiral **2**. The transfer of asymmetry is maximum in equimolar mixtures of **1b** and **2** (Fig. S22b, ESI†). Furthermore, the low intensity of the dichroic response could be attributed to the small number of aggregated molecules due to the anti-cooperative mechanism.

The formation of **1-co-2** species in solution was also investigated by SAXS measurements at different concentrations. In good analogy with the data derived from pristine **1** and **2**, the SAXS profiles of **1a-co-2** and **1b-co-2** are fitted to monodisperse elliptical cylinders with a minor radius of ~1 nm (axis ratios ~2) and lengths ranging from 3.2 to 6.6 nm (Table S2 and Fig. S23, ESI†). Finally, the formation of short aggregates upon the co-assembly of **1a** with the BODIPY derivative **2** was visualized by AFM imaging. Similar to the aggregates of **1a** and **2**, short, curly fibrillar aggregates, with typical heights of ~2 nm, are visualized (Fig. S24, ESI†). All these experimental results indicate that the anti-cooperative supramolecular polymerization shown by the pristine components also governs the growth of the small co-assembled aggregates formed by the BDT and BODIPY derivatives.

Conclusions

We describe herein the anti-cooperative supramolecular polymerization by attenuated growth exhibited by self-assembling units of two BDT derivatives (**1a** and **1b**) and BODIPY (**2**). The three systems display non-sigmoidal curves in VT-UV-Vis experiments indicating a cooperative supramolecular polymerization mechanism. Unexpectedly, both AFM imaging and SAXS measurements reveal the formation of small aggregates that suggests the operation of an anti-cooperative mechanism strongly conditioned by attenuated growth, in which the formation of a nucleus is favoured over the subsequent addition of monomeric units to the aggregate. Theoretical calculations show that both the BDT and BODIPY motifs, upon the favourable formation of the initial dimeric nuclei, experience a strong distortion of the central aromatic core upon growth. This distortion destabilizes the resulting supramolecular polymer and disfavours the addition of subsequent monomer units, thus impeding the formation of long fibrillar structures. Finally, despite the anti-cooperativity observed in the supramolecular polymerization of compounds **1** and **2**, the combination of both self-assembling units results in the formation of small co-assembled aggregates with a similar supramolecular polymerization behaviour to that observed for the separate components. This study contributes to expanding the knowledge on anti-cooperative supramolecular polymerization and provides a useful strategy to achieve functional, oligomeric supramolecular species of different lengths thus bridging the gap between molecular and macromolecular levels.

Data availability

All the experimental data have been included in the ESI.†

Author contributions

Yeray Dorca, Cristina Naranjo, and Goutam Ghosh: investigation, methodology, visualization, and writing. Bartolomé Soberats: SAXS measurements and writing; Joaquín Calbo: theoretical calculations and writing; Enrique Ortí, Gustavo Fernández, and Luis Sánchez: conceptualization, writing, supervision, and funding acquisition.

Conflicts of interest

There are no conflicts to declare.

Acknowledgements

Financial support by the MICINN of Spain (PID2020-113512GB-I00, PGC2018-099568-B-I00, RED2018-102331-T and Unidad de Excelencia María de Maeztu CEX2019-000919-M), the Generalitat Valenciana (PROMETEO/2020/077), the Comunidad de Madrid (NanoBIOCARGO, P2018/NMT-4389), and European Feder funds (PGC2018-099568-B-I00) is acknowledged. C. N. is grateful to Comunidad de Madrid for her predoctoral fellowship.

Notes and references

1 (*a*) T. F. A. De Greef, M. M. J. Smulders, M. Wolffs, A. P. H. J. Schenning, R. P. Sijbesma and E. W. Meijer, *Chem. Rev.*, 2009, **109**, 5687; (*b*) H. M. M. ten Eikelder and A. J. Markvoort, *Acc. Chem. Res.*, 2019, **52**, 3465.
2 M. Wehner and F. Würthner, *Nat. Rev. Chem.*, 2020, **4**, 38.
3 T. Aida, E. W. Meijer and S. I. Stupp, *Science*, 2012, **335**, 813.
4 G. Ghosh, P. Dey and S. Ghosh, *Chem. Commun.*, 2020, **56**, 6757.
5 P. A. Korevaar, S. J. George, A. J. Markvoort, M. M. J. Smulders, P. A. Hilbers, A. P. H. J. Schenning, T. F. A. de Greef and E. W. Meijer, *Nature*, 2012, **481**, 492.
6 J. Matern, Y. Dorca, L. Sánchez and G. Fernández, *Angew. Chem., Int. Ed.*, 2019, **58**, 16730.
7 A. Aliprandi, M. Mauro and L. De Cola, *Nat. Chem.*, 2016, **8**, 10.
8 E. E. Greciano, J. Calbo, E. Ortí and L. Sánchez, *Angew. Chem., Int. Ed.*, 2020, **59**, 17517.
9 M. Wehner, M. I. S. Röhr, M. Bühler, V. Stepanenko, W. Wagner and F. Würthner, *J. Am. Chem. Soc.*, 2019, **141**, 6092.
10 J. B. Gilroy, T. Gädt, G. R. Whittell, L. Chabanne, J. M. Mitchels, R. M. Richardson, M. A. Winnik and I. Manners, *Nat. Chem.*, 2010, **2**, 566.
11 S. Ogi, K. Sugiyasu, S. Manna, S. Samitsu and M. Takeuchi, *Nat. Chem.*, 2014, **6**, 188.
12 J. Kang, D. Miyajima, T. Mori, Y. Inoue, Y. Itoh and T. Aida, *Science*, 2015, **347**, 646.
13 S. Ogi, V. Stepanenko, K. Sugiyasu, M. Takeuchi and F. Würthner, *J. Am. Chem. Soc.*, 2015, **137**, 3300.
14 Y. Liu, C. Peng, W. Xiong, Y. Zhang, Y. Gong, Y. Che and J. Zhao, *Angew. Chem., Int. Ed.*, 2017, **56**, 11380.
15 J. S. Valera, R. Gómez and L. Sánchez, *Small*, 2018, **14**, 1702437.
16 E. E. Greciano, B. Matarranz and L. Sánchez, *Angew. Chem., Int. Ed.*, 2018, **57**, 4697.
17 B. Adelizzi, N. J. Van Zee, L. N. De Windt, A. R. A. Palmans and E. W. Meijer, *J. Am. Chem. Soc.*, 2019, **141**, 6110.
18 H. Frisch, E.-C. Fritz, F. Stricker, L. Schmüser, D. Spitzer, T. Weidner, B. J. Ravoo and P. Besenius, *Angew. Chem., Int. Ed.*, 2016, **55**, 7242.
19 E. Ressouche, S. Pensec, B. Isare, G. Ducouret and L. Bouteiller, *ACS Macro Lett.*, 2016, **5**, 244.
20 D. Görl, X. Zhang, V. Stepanenko and F. Würthner, *Nat. Commun.*, 2015, **6**, 7009.
21 W. Zhang, W. Jin, T. Fukushima, A. Saeki, S. Seki and T. Aida, *Science*, 2011, **334**, 340.
22 S. H. Jung, D. Bochicchio, G. M. Pavan, M. Takeuchi and K. Sugiyasu, *J. Am. Chem. Soc.*, 2018, **140**, 10570.
23 B. Adelizzi, A. Aloi, A. J. Markvoort, H. M. M. Ten Eikelder, I. K. Voets, A. R. A. Palmans and E. W. Meijer, *J. Am. Chem. Soc.*, 2018, **140**, 7168.
24 W. Zhang, W. Jin, T. Fukushima, T. Mori and T. Aida, *J. Am. Chem. Soc.*, 2015, **137**, 13792.
25 S. H. Jung, D. Bochicchio, G. M. Pavan, M. Takeuchi and K. Sugiyasu, *J. Am. Chem. Soc.*, 2018, **140**, 10570.
26 A. Sarkar, R. Sasmal, C. Empereur-Mot, D. Bochicchio, S. V. K. Kompella, K. Sharma, S. Dhiman, B. Sundaram, S. S. Agasti, G. M. Pavan and S. J. George, *J. Am. Chem. Soc.*, 2020, **142**, 7606.
27 B. Adelizzi, P. Chidchob, N. Tanaka, B. A. G. Lamers, S. C. J. Meskers, S. Ogi, A. R. A. Palmans, S. Yamaguchi and E. W. Meijer, *J. Am. Chem. Soc.*, 2020, **142**, 16681.
28 A. Arnaud, J. Belleney, F. Boué, L. Bouteiller, G. Carrot and V. Wintgens, *Angew. Chem., Int. Ed.*, 2004, **43**, 1718.
29 (*a*) J. Gershberg, F. Fennel, T. H. Rehm, S. Lochbrunner and F. Würthner, *Chem. Sci.*, 2016, **7**, 1729; (*b*) Y. Vonhausen, A. Lohr, M. Stolte and F. Würthner, *Chem. Sci.*, 2021, **12**, 12302.
30 K. Cai, J. Xie, D. Zhang, W. Shi, Q. Yan and D. Zhao, *J. Am. Chem. Soc.*, 2018, **140**, 5764.
31 L. Herkert, J. Droste, K. K. Kartha, P. A. Korevaar, T. F. A. de Greef, M. R. Hansen and G. Fernández, *Angew. Chem., Int. Ed.*, 2019, **58**, 11344.
32 (*a*) P. Besenius, G. Portale, P. H. H. Bomans, H. M. Janssen, A. R. A. Palmans and E. W. Meijer, *Proc. Natl. Acad. Sci. U. S. A.*, 2010, **107**, 17888; (*b*) R. Appel, J. Fuchs, S. M. Tyrrell, P. A. Korevaar, M. C. A. Stuart, I. K. Voets, M. Schçnhoff and P. Besenius, *Chem.–Eur. J.*, 2015, **21**, 19257; (*c*) R. van der Weegen, P. A. Korevaar, P. Voudouris, I. K. Voets, T. F. A. de Greef, J. A. J. M. Vekemans and E. W. Meijer, *Chem. Commun.*, 2013, **49**, 5532.
33 L. Huo and J. Hou, *Polym. Chem.*, 2011, **2**, 2453.
34 G. Ulrich, R. Ziessel and A. Harriman, *Angew. Chem., Int. Ed.*, 2008, **47**, 1184.
35 M. J. Mayoral, D. Serrano-Molina, J. Camacho-García, E. Magdalena-Estirado, M. Blanco-Lomas, E. Fadaei and D. González-Rodríguez, *Chem. Sci.*, 2018, **9**, 7809.
36 A. Rödle, B. Ritschel, C. Mück-Lichtenfeld, V. Stepanenko and G. Fernández, *Chem.–Eur. J.*, 2016, **22**, 15772.
37 F. C. Spano and C. Silva, *Annu. Rev. Phys. Chem.*, 2014, **65**, 477.
38 H. M. M. ten Eikelder, A. J. Markvoort, T. F. A. de Greef and P. A. J. Hilbers, *J. Phys. Chem. B*, 2012, **116**, 5291.
39 D. S. Philips, K. K. Kartha, A. T. Politi, T. Krüger, R. Q. Albuquerque and G. Fernández, *Angew. Chem., Int. Ed.*, 2019, **58**, 4732.
40 E. E. Greciano, S. Alsina, G. Ghosh, G. Fernández and L. Sánchez, *Small Methods*, 2020, **4**, 1900715.
41 Y. Xiong, M. Wang, X. Qiao, J. Li and H. Li, *Tetrahedron*, 2015, **71**, 852.

42 A. Maity, A. Sarkar, A. Sil, B. N. S. Bhaktha and S. K. Patra, *New J. Chem.*, 2017, **41**, 2296.
43 R. Draper, B. Dietrich, K. McAulay, C. Brasnett, H. Abdizadeh, I. Patmanidis, S. J. Marrink, H. Su, H. Cui, R. Schweins, A. Seddon and D. J. Adams, *Matter*, 2020, **2**, 764.
44 C. Bannwarth, S. Ehlert and S. Grimme, *J. Chem. Theory Comput.*, 2019, **15**, 1652.
45 The reliability of the dimer relative energies calculated at the GFN2-xTB level was confirmed by performing DFT-B3LYP + D3/6-31G(d,p) calculations (see Table S3†).
46 The preference of a linear stack with weakly-directional H-bonds over the helical arrangement is maintained upon inclusion of continuum environment effects with a variety of solvents (see ESI†).
47 A. Sarkar, T. Behera, R. Sasmal, R. Capelli, C. Empereurmot, J. Mahato, S. S. Agasti, G. M. Pavan, A. Chowdhury and S. J. George, *J. Am. Chem. Soc.*, 2020, **142**, 11528.
48 Y. Yamamoto, T. Fukushima, Y. Suna, N. Ishii, A. Saeki, S. Seki, S. Tagawa, M. Taniguchi, T. Kawai and T. Aida, *Science*, 2006, **314**, 1761.
49 M. Sarma and K.-T. Wong, *ACS Appl. Mater. Interfaces*, 2018, **10**, 19279.